

The mechanics and temporal evolution of an open-system magmatic intrusion into a crystal-rich magma

J. M. Schleicher and G. W. Bergantz*

Department of Earth and Space Sciences, University of Washington, Seattle, WA 98195, USA

*Corresponding author. Telephone: 206-685-4972. E-mail: bergantz@uw.edu

Received February 9, 2017; Accepted July 12, 2017

ABSTRACT

Magma reservoirs reside primarily in crystal-rich states, yet plutonic and volcanic examples indicate that rapid open-system cycling is common, as expressed in complex crystal zonation. Open-system magmatic events can fluidize crystal-rich magma (mush), but the dynamics of these events are poorly understood. We employ discrete element method-computational fluid dynamics simulations of the intrusion of a basaltic liquid into an olivine-basaltic mush to reveal the hydrogranular controls and kinematic states during a momentum-driven, open-system event. Three stages are described: (1) the initial response of the mush, characterized by viscoplastic expansion along crystal-liquid faults enclosing a fluidized region we call the mixing bowl; (2) the quasi steady state stage, where the intruding liquid transits the mixing bowl as a crystal-poor chimney and generates crystal-liquid mixing by a combination of vertical transport and overturn in granular vortices; (3) the termination of the open-system event, where crystals settle and slump into a packed state. The local crystal-liquid Viscous number and the time-dependent average crystal coordination number rationalize the presence of multiple hydrogranular dynamic regimes. Using a boundary layer based kinetic law we find that the crystals experience dissolution rates of $\sim 10 \mu\text{m h}^{-1}$. These rates fall within the range of values for olivine dissolution previously determined by experimental and theoretical studies. The presented simulation demonstrates that most crystal and liquid mixing occurs within the fluidized mixing bowl. The hydrogranular controls on crystal and liquid motion have the potential to create a diverse crystal cargo during a single open-system event, even in a geologically simple system.

Key words: crystal-rich magmas; fluidization; granular dynamics; magma mixing; open-system intrusion

INTRODUCTION

Magma reservoirs are dominated by near-solidus, high crystal-fraction conditions (known as a magmatic mush) for tens of thousands to millions of years (Reid, 2008; Schmitt, 2011; Cooper, 2015). Yet complexly zoned crystals erupted from crystal-rich magmas require rapid mobilization, occurring on timescales over days to hundreds of years (Costa & Morgan, 2011; Kahl *et al.*, 2011, 2013; Moore *et al.*, 2014; Cooper, 2015; Shea *et al.*, 2015; Cooper *et al.*, 2016). Open-system intrusions of magma into magmatic mushes can rapidly disaggregate and mobilize the near-solidus magma,

and explain the eruption of distinct populations of crystals (Wallace & Bergantz, 2005; Ruprecht *et al.*, 2008; Streck, 2008; Girard & Stix, 2009; Burgisser & Bergantz, 2011; Kahl *et al.*, 2011; Huber *et al.*, 2012; Thomson & MacLennan, 2013; Bergantz *et al.*, 2015) and crystals out of equilibrium with their carrier liquids (Passmore *et al.*, 2012; Neave *et al.*, 2013; Moore *et al.*, 2014). However, the mechanics and temporal evolution of an open-system intrusion are not well understood (Bergantz & Breidenthal, 2001). Geological examples demonstrate that intruded magma can percolate or pond in the

resident mush (Perugini & Poli, 2005; Paterson, 2009; Costa *et al.*, 2010), or can lead to mush disaggregation and eruption (Kahl *et al.*, 2011; Passmore *et al.*, 2012; Thomson & Maclennan, 2013).

The presence of crystals greatly affects the mechanics of a magma through both hydrodynamic and granular interactions (Marsh, 1981). Crystal concentrations of as little as 25 vol. % can form crystal contact networks (Philpotts *et al.*, 1999), which can cause jamming, strain localization, variable crystal packing, and the transmission of stress by crystal–crystal contacts called force chains (Sun *et al.*, 2010; Sandnes *et al.*, 2011; Estep & Dufek, 2012). There are several mechanisms that can lead to the fluidization of crystals within a mush, including gas-driven overturn (Ruprecht *et al.*, 2008), buoyancy-driven overturn from basal intrusion and heating (Girard & Stix, 2009; Burgisser & Bergantz, 2011; Huber *et al.*, 2012), and momentum-driven fluidization by magmatic intrusions (Bergantz *et al.*, 2015). An open-system, momentum-driven intrusion can fluidize a crystal-rich mush when the intruding liquid locally separates contacts between crystals. This creates locally dilute (higher porosity) regions of the mush, which behave as a mobile fluid rather than a viscoplastic solid.

Investigating the mechanics involved in an open-system intrusion requires an approach that resolves both the crystal-scale and the mush-scale throughout the event. We present a discrete element method–computational fluid dynamics (DEM–CFD) simulation to examine the granular and fluid dynamics of basaltic liquid intruding into an olivine-rich basaltic mush. The particle-based numerical modeling is described in the Supplementary Data (available for downloading at <http://www.petrology.oxfordjournals.org>) and includes frictional, collisional, translational, and buoyant forces, as well as viscous particle–particle–fluid coupling. This approach reveals the microphysical controls on fluidization and mixing in a mush over a range of spatial scales simultaneously, which cannot be resolved with continuum modeling (mixture or Eulerian–Eulerian multi-fluid theories). The particle-based simulation records the motion of all crystals within the mush, allowing us to examine crystal gathering and dispersal during the intrusion.

We have described some general features of magma dynamics using the DEM–CFD method in two previous publications. In Bergantz *et al.* (2015) we introduced the notion of the ‘mixing bowl’ but did not describe the distinct time-dependent regimes throughout an open-system cycle. In Schleicher *et al.* (2016) we described how crystal mixing could be quantified. Here we document and describe the distinct kinematic stages of an open-system event in a magma mush, and present a scaling to describe the multiphase dynamics under crystal-rich conditions. We also monitor the mixing between the crystals and the resident and intruding liquids, and their potential for recording the intrusion with crystal growth or dissolution.

Table 1: Simulation parameters

| Parameter (units) | Variables | Values |
|---|------------|------------|
| Domain size (m) | D_w, D_h | 2.56, 1.28 |
| Computational grid size (m) | | 0.01, 0.01 |
| Injection width (m) | l_w | 0.32 |
| Liquid density (kg m^{-3}) | ρ_l | 2650 |
| Liquid dynamic viscosity (Pa s) | μ_l | 0.2 |
| Crystal density (kg m^{-3}) | ρ_c | 3300 |
| Crystal diameter (m) | d_c | 0.004 |
| Initial bed height (m) | H_0 | 0.823 |
| Number of crystals | N | 147040 |
| Simulation time (s) | t | 100 |
| Injection velocity (m s^{-1}) | U_0 | 0.023 |
| Minimum fluidization velocity (m s^{-1}) | U_{mf} | 0.0025 |
| Mixing bowl taper angle from the vertical (radians) | α | $\pi/6$ |

MULTIPHASE SIMULATION OF AN INTRUDED MAGMATIC MUSH

To exemplify the mechanics of an open-system intrusion, we consider a geologically simple, yet common crystal-rich system: an olivine-mush in basaltic liquid (Table 1). To create the mush, we randomly distribute olivine crystals throughout the domain and allow them to settle. Crystals naturally organize into a random loose-packed bed, creating an average crystal fraction of ~ 0.6 . We saturate the crystals with a resident liquid, which extends above the bed into a crystal-free region. An intruding, crystal-free liquid enters the mush as a dike into the base of the domain at a constant momentum flux. The properties of the resident and intruding liquids are the same, approximating conditions observed in basalts (Table 1); calculations with MELTS indicated that melt density changed only 0.6% over the 50 degree temperature interval assumed here and so will have negligible influence on the dynamics. Basaltic systems are often intruded by liquids with similar temperatures, viscosities, and densities to those residing within the mush (Rhodes, 1988; Geist *et al.*, 2006), therefore all simulations are run with isothermal conditions. The open-system nature of the intrusion requires a domain where liquid is allowed to leave the top to accommodate the constant momentum flux of the intruding liquid. This assumption is supported by geological examples where input can be accommodated by crustal deformation (Gerbi *et al.*, 2004; Baker & Amelung, 2012). Additionally, magma can drain from cracks in the crust above magma reservoirs, allowing intruding magma to fill in the void spaces without accompanying crustal deformation (Johnson *et al.*, 2010). The walls and base of the domain have a no-slip boundary condition for the liquid, and a wall-friction law for the crystals. The majority of liquid and crystal motions occur far from the walls, so boundaries have little influence on the overall dynamics of the system. Simulations are 2.5-D, with the depth of the domain given by the diameter of the crystals. However, this value is much less than the other spatial dimensions in the system, creating an

effectively 2-D system. The theory and equations describing the numerical simulations can be found in the Supplementary Data.

MECHANICAL FLUIDIZATION OF MAGMATIC MUSHES

The general concept of fluidization as used in industry and sedimentary geology refers to the support of a bed of particles by the upward drag exerted by a fluid. The fluid works against gravity, expanding and supporting the bed from a stationary rest state. To fluidize a crystal-rich mush, the intruding liquid must enter at a sufficient rate to overcome the weight of the crystal bed. This rate is known as the minimum fluidization velocity (U_{mf}), which is commonly calculated using the Ergun equation (Ergun, 1952). This equation for the minimum fluidization velocity estimates the velocity of the injected liquid needed to induce a drag force on the crystals equaling the weight of the crystals. In these calculations, the work needed to overcome initial contact friction between the crystals is ignored.

Scaling model variables for applications to natural examples

The application of a model to natural examples requires scaling variables to ensure consistent extension of model results to other similar applications. Hence, the thermophysical properties and the system geometry need to be represented in terms of scaled quantities. In the case of our model of a crystal mush, these are the size of the crystals, the liquid viscosity, the thickness of the bed, and the rate of the incoming new intrusion that acts as to fluidize the crystal bed. One quantity that embodies all these degrees of freedom is the minimum fluidization velocity. In our simulations, liquid intrudes only a portion of the base of the crystal bed. We also know from our results described below that the fluidization occurs as a tapered geometry, an emergent property of the calculations, and we apply that *ex post facto* to ensure the proper scaling. Because of this, the Ergun equation must be modified to account for only the crystals that are fluidized in the region above the intrusion. As in Bergantz *et al.* (2015) and Schleicher *et al.* (2016), we use a modified U_{mf} calculation in our simulations, which accounts for the small injection region relative to the domain size (Cui *et al.*, 2014):

$$\frac{1}{2} \alpha B l_w^2 \ln \left(\frac{2H_0}{l_w} \right) U_{mf}^2 + \alpha A l_w \left(H_0 - \frac{l_w}{2} \right) U_{mf} \quad (1)$$

$$= (l_w + H_0 \tan \alpha) H_0 (\rho_c - \rho_l) g (1 - \varepsilon_l) \quad (2)$$

$$A = 150 \left(\frac{1 - \varepsilon_l}{\varepsilon_l^3} \right)^2 \frac{\mu_l}{d_c^2}$$

$$B = 1.75 \left(\frac{1 - \varepsilon_l}{\varepsilon_l^3} \right) \frac{\rho_l}{d_c}. \quad (3)$$

In these equations, α is the angle from the vertical formed by the tapered geometry of the mixing bowl

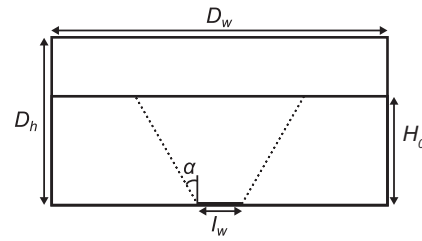


Fig. 1. Schematic illustration of the simulation domain (D_w is width, D_h is height) and emergent mixing bowl, illustrating the variables used in equations (1)–(3).

(Fig. 1), l_w is the width of the injection region, H_0 is the height of the crystal–liquid bed, U_{mf} is the minimum fluidization velocity, ε_l is the liquid fraction (porosity), μ_l is the dynamic viscosity of the liquid, ρ_l is the liquid density, d_c is the crystal diameter, ρ_c is the crystal density, and g is the magnitude of gravitational acceleration.

Only one intrusion rate is exemplified in our detailed example presented here; however, varied intrusion rates of the intruded liquid change the emergent behavior of the mush (Schleicher *et al.*, 2016). We introduce a non-dimensional velocity U^* , which is the injected velocity of the liquid (U_0) divided by the U_{mf} of the mush ($U^* = U_0/U_{mf}$). At low intrusion rates ($U^* \ll 1$), the liquid is unable to fluidize the crystals and passes through the mush by porous flow. Intermediate intrusion rates ($U^* \sim 1$) create a short, crystal-poor cavity, and higher intrusion rates ($U^* > 1$) extend the cavity into a chimney (Philippe & Badiane, 2013). In magmatic systems, open-system intrusions may occur with liquid rising slowly through the mush, passing through the crystals as porous flow ($U^* < 1$). Examples of this exist in Iceland and in other rift zone systems (Costa *et al.*, 2010; Thomson & MacLennan, 2013). Other intrusions can enter the mush with sufficient momentum to fluidize the crystals ($U^* > 1$), leading to mixing and possibly eruption (Passmore *et al.*, 2012; Neave *et al.*, 2013; Moore *et al.*, 2014).

THE CYCLE OF AN OPEN-SYSTEM INTRUSION EVENT

Below we describe the three stages that a model crystal-rich mush might experience during an open-system event where a portion of the resident mush is fully fluidized. These stages correspond to (1) the initial response of the mush to the intrusion, (2) the self-similar, quasi steady state stage, and (3) the shut-off stage at the end of the open-system event. Distinct multiphase regimes can exist simultaneously during these stages of the intrusion as a result of the changing particle volume fraction (Jaeger *et al.*, 1996; Andreotti *et al.*, 2013). The highest particle fraction regime (≥ 0.5) is called the quasi-static state, where particles are in constant frictional and normal contact. Relative particle motion occurs by particle translation governed by the inter-particle geometry (Roux, 2009). At intermediate volume fractions (~ 0.5 – 0.1) is the dense granular

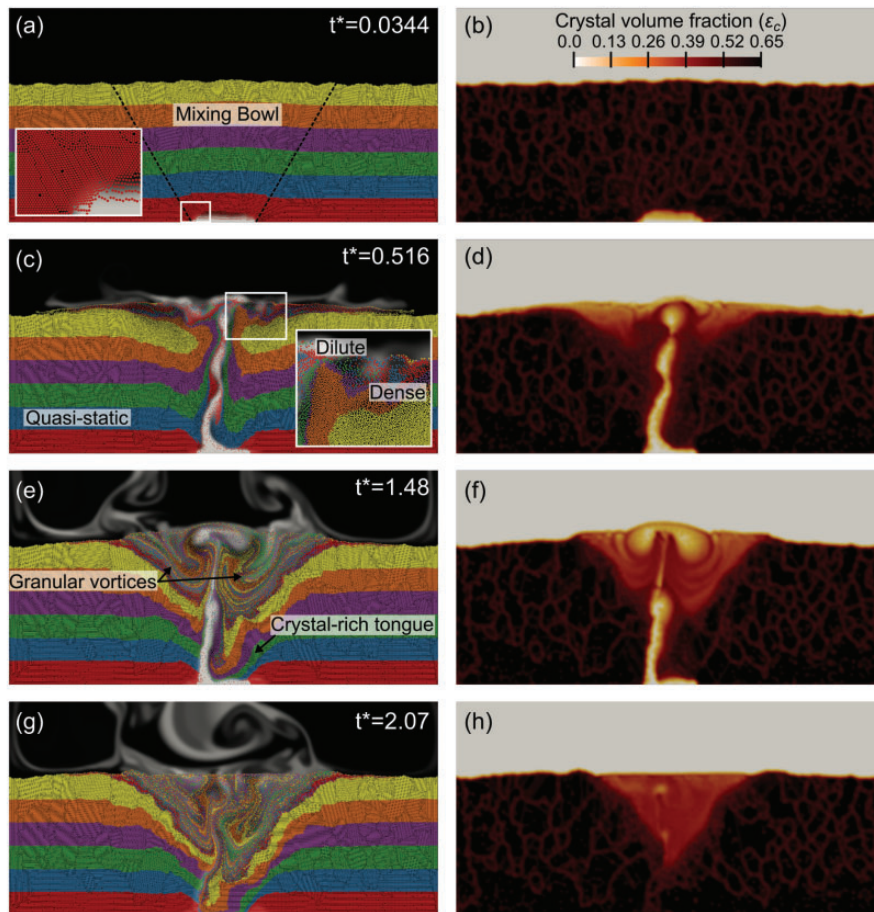


Fig. 2. Four time steps from the simulation of the open-system intrusion, where $t^* = (U_0/H_0)t$. (a), (c), (e), and (g) show the crystals (colored bands) and liquids (black for resident liquid; white for intruding liquid); (b), (d), (f), and (h) show the crystal volume fraction for the same times. Black dashed lines in (a) represent the extent of the mixing bowl and inset image shows the lines of crystals forming the granular faults. Color bar in (b) illustrates the crystal volume fraction. The variations in crystal volume fraction within the bed represent the variable packing of the crystals from the initial random settling. (See text for additional description and details.)

regime (MiDi, 2004; Jop, 2015) where particles are fluidized, but frequent contacts between particles may be sustained (frictional) or collisional. At very low particle fractions (<0.1) the granular flow is in the dilute regime, where particle contacts are infrequent, and momentum is exchanged by collisions (Goldhirsch, 2003). These three granular regimes express the diversity of mechanical behavior exhibited by the mush throughout an open-system cycle. A video of the simulation can be viewed in the online Supplementary Data (Movie 1).

Initially fluidizing the mush by intrusion of new magma

When the new magma intrudes the resident crystal-rich mush, the mush responds as a viscoplastic material. The initial crystal packing in the bed ($\epsilon_c \sim 0.6$) results in continuous contact between crystals (i.e. the quasi-static granular regime). Slight variation in crystal volume fraction exists in the bed (Fig. 2b), which is the result of natural settling of the crystals to form the mush. At the start of the intrusion, pore pressure created from the intruding liquid exceeds the frictional yield strength of the mush;

the viscoplastic response of the mush includes vertical expansion and simultaneous fluidization along bounding crystal-liquid faults (Fig. 2a). We use the term ‘fault’ because the initial failure is one involving frictional forces, there is manifest material displacement across the interface, the interfaces persist with minor erosion along the surfaces, and the faults are at approximately 60° angles to the horizontal on both sides of the intrusion, as predicted by Mohr–Coulomb failure criteria. They are faults, rather than shear zones. At the crystal scale, each fault is not a single plane (line, in the case of the 2D simulation), but a band of crystals moving along 60° angles from the horizontal (see inset image in Fig. 2a). The crystal networks can be ~ 10 – 100 crystals long, and the lateral extent of the crystals creating the macroscopic faults can be ~ 10 – 20 crystals wide. The faults delimit the region of the mush that is unlocked by fluidization, and this region is referred to as the ‘mixing bowl’.

The geometry of the mixing bowl is established by this initial response and is insensitive to changes in intrusion rates exceeding the U_{mf} . In this simulation the intrusion rate is 9.26 times the U_{mf} ($U^* = 9.26$). The

mixing bowl is a robust feature indicating that the numerical experiments satisfy the criteria for a self-similar extensible result. For example, varying the mush height does not alter the angle of the faults delimiting the mixing bowl, even when the height of the bed is less than half the width of the intrusion. As shown later in the simulation, most of the mixing that occurs in the mush is within the mixing bowl, the only portion of the mush that is mobilized.

The initial viscoplastic response of the mush is followed by block uplift of the resident mush within the mixing bowl, similar to experiments by [Johnsen *et al.* \(2008\)](#). After the initial uplift, the intruding liquid forms a small crystal-poor cavity that breaks up into finger-like instabilities as penetrative convection of the new liquid enters the mush. Around each instability is a halo of fluidized crystals that propagates ahead of the intruding liquid. The fingers do not rise at the same rate, and the shear stress at their margins entrains them together to form a single, rising, crystal-poor feature (these dynamic features are best seen in the Supplementary Data Movie 1). The length scales of this process are not recoverable by Saffman–Taylor viscous scaling (where less viscous material intrudes more viscous material) owing to intermittent flow from particle jamming ([Sandnes *et al.*, 2011](#)). The rising intruding liquid entrains crystals from the base of the mush and carries them upwards to the top of the crystal bed. This crystal–fluid coupling hinders the formation of lasting crystal contacts, placing the low-crystal fraction instability within the dilute granular regime ([Burgisser *et al.*, 2005](#); [Andreotti *et al.*, 2013](#)).

Once the initial instability has penetrated the entire mush the initial transient ends, leaving a feature we call the chimney ([Fig. 2c](#) and [d](#)). The chimney is a region of continued throughput and high porosity, surrounded by variably fluidized mush. Outside the dilute chimney, the mixing bowl remains in the quasi-static regime where the crystal volume fraction is close-packed. The upper portion of the mixing bowl has a lower crystal volume fraction and is in the dense granular regime.

The self-similar mixing bowl

After the initial transient described above, the dynamics in the mixing bowl are governed by quasi steady state, self-similar behavior ([Fig. 2e](#)) (self-similar describes an object or condition whose proportions remain the same as it becomes larger or smaller; the features are scale invariant). The approximate geometry of the mixing bowl persists, although there is minor crystal transport from erosion of the bounding granular faults. The dominant feature within the mixing bowl is the crystal-poor chimney. Throughout the intrusion, the chimney rises through the mush with varicose and meandering instabilities ([Huppert *et al.*, 1986](#)). These forms of instability reflect the moderate Reynolds numbers (~ 10 – 100) of the chimney as it moves through the mush [see [fig. 7](#) of [Huppert *et al.* \(1986\)](#)]. The varicose instabilities cause

liquid to arrive at the top of the mush in pulses, creating local variations in crystal fraction within the dense granular regions at the top of the mixing bowl ([Fig. 2f](#)).

As the crystal-poor liquid rises through the mush, it entrains crystals from the base of the mixing bowl and the sides of the chimney. These crystals are carried to the top of the mush and deposited on either side of the chimney, while the chimney liquid bifurcates and rises to mingle with the resident liquid above the mush. The entrainment, vertical transport, and deposition of crystals by the chimney create counter-rotating ‘granular vortices’ that mix the crystals and liquid at the top of the mixing bowl. The overturn time of these granular vortices is approximately the same as the transit time of a crystal through the entire chimney. Owing to the meandering chimney, the vortices are not perfectly symmetric within the mixing bowl. However, the persistent fluidization of the mixing bowl maintains a self-similar geometry. In addition to upwards translation of crystals by the chimney, coherent tongues of crystals move downwards along the crystal–liquid faults of the mixing bowl. This continued upwards and downwards motion of the crystals extends the well-mixed portion of the mixing bowl towards the intrusion site. We have previously shown ([Schleicher *et al.*, 2016](#)) that the majority of the crystals within the entire mixing bowl eventually become well mixed.

Termination of the intrusion and defluidization of the mush

Once the new magma input is terminated, the mixing bowl begins to defluidize and collapse ([Fig. 2g](#) and [h](#)). The collapse happens rapidly at the bottom, where low-porosity, crystal-rich tongues slump into the former location of the chimney, re-establishing a quasi-static regime. This rapid collapse hinders additional mixing of the liquids, so a fossil chimney of intruded liquid remains. In the higher porosity core of the mixing bowl, the re-establishment of the close-packed mush occurs as hindered crystal settling. The top of the mixing bowl has a concave-up shape with pronounced shoulders, which formed as some crystals were transported out of the mixing bowl during the intrusion. Once the crystals have returned to a settled state, the mixing bowl will have a fossil kinematic and compositional character, distinct from the surrounding mush that was undisturbed by the intrusion.

GRANULAR MECHANICS AND THE VISCOUS AND COORDINATION NUMBERS

The three stages of the open-system event described above demonstrate the complexity of dynamic states that can be manifested by multiphase systems with high particle concentrations. Multiple hydrogranular regimes are present at any given time during the simulation; these regimes are distinguished by the local particle fraction, the timescales involved with particle

motion, and the shear rate. This is because the transmission of force by hydrogranular interactions has numerous sources: collisions, enduring frictional contact, lubrication, and fluid viscous effects. This is especially the case in particle-rich systems such as those considered here, where the forces and particle support are transmitted along quasi-linear force chains that appear stochastically (Cates *et al.*, 1998; Sun *et al.*, 2010; Estep & Dufek, 2012). This produces a support fabric composed of load-bearing particles and spectators (Cates *et al.*, 1998; Sun *et al.*, 2010; Estep & Dufek, 2012). The force chains that form the support fabric migrate in response to external forcing, such that a particle that is a spectator one moment may be load-bearing the next. Even in simple, unimodal mixtures this can often produce non-affine deformation and non-local conditions such that the stress at a point depends on the degree of mobility in the surroundings as well as the shear rate (Trulsson *et al.*, 2012).

One system property that has been invoked for distinguishing mechanical states is the critical crystal fraction associated with jamming ($\varepsilon_{c,c}$) (Marsh, 1981). A thorough discussion of jamming, which progresses through a succession of micro- and macrofragile states (Cates *et al.*, 1998; Ness & Sun, 2016) to hard jamming when a critical shear stress (not shear rate) is exceeded (Peters *et al.*, 2016), is beyond the scope of this work, so we simply adopt the findings of Ness & Sun (2015), where a threshold particle fraction for monodisperse spherical particles occurs between 0.57 and 0.59. The highest particle fractions define the quasi-static regime, where particle contacts are enduring and frictional contact is the primary mechanism of force transmission. The dense granular regime is challenging to generalize with a bulk rheology, as the behavior depends not only on volume fraction, but also sample preparation (Daerr & Douady, 1999), confining pressure, and shear rate (da Cruz *et al.*, 2005). Once the system reaches $\varepsilon_{c,c}$, the granular media macroscopically behaves as a plastic material, controlled by a friction criterion with a linear relationship between shear and normal stresses.

Despite this complexity, remarkably, the same approach that has been useful in illuminating the fundamental controls on dilute multiphase flow (Burgisser *et al.*, 2005) can be employed in high-particle fraction conditions. That is, the microscopic response timescale of a single particle relative to the macroscopic timescale of the far-field forces acting on that particle can rationalize the multiphase physics. For example, in the context of dilute flow, this is the ratio of the microscopic aerodynamic response time of a particle to the time a macroscopic carrier phase (fluid in this case) exerts a distinct force on it. This led to the introduction of a Stokes number, which is the ratio of those two timescales. If the Stokes number is low the particle follows the fluid as a tracer, whereas if the Stokes number is high the particle is not bound to the fluid motion and is acting as a ballistic particle in the inertial state (Burgisser *et al.*, 2005).

The same notions of a particle response timescale relative to the behavior of the carrier phase emerge in dense multiphase flow (du Pont *et al.*, 2003; Cassar *et al.*, 2005). The premise is that particles exist in a granular framework where particle–particle contacts are idealized as points, and where force is collectively transmitted in a ‘granular continuum’. The mechanical connection between a particle and its neighbors is quantified by the particle coordination number, Z , which is a count of all the contacts between a particle and its neighbors. Conceptually, this granular continuum plays the same role in controlling the macroscopic scales as the fluid in dilute flows. Now if the granular framework is sheared, a particle can be displaced from its initial position and coordination state by macroscopic forces working against a microscopic restoring gravitational force (or some general restoring pressure for neutrally buoyant crystals), which will act to return it to the previous location. If the macroscopic forces acting on the particle carry it beyond its original location before the particle can re-establish contact with its neighbors in the granular continuum, the coordination number will approach zero. In this scenario, the particle is effectively an inertial or ballistic particle (even at low particle-Reynolds number), with respect to the granular continuum, just as in the dilute case. This leads to a disassociation of the granular continuum, a reduction in the local particle volume fraction and a decrease in the number density of force chains.

The particle–fluid coupling can be quantified by the value of a Viscous number (l_v), where it is assumed that the particle response time is governed by viscous forces (Trulsson *et al.*, 2012; Ness & Sun, 2015):

$$l_v = \frac{3\mu_l \dot{\gamma}}{2(\rho_c - \rho_l)gd_c}. \quad (4)$$

Here μ_l is the dynamic viscosity of the liquid, $\dot{\gamma}$ is the local shear rate of the liquid (calculated at the computational-cell scale), ρ_c and ρ_l are the densities of the crystals and liquid, respectively, g is the gravitational acceleration, and d_c is the diameter of the crystals. As in dilute flows, a value of $l_v \ll 1$ indicates that the particle will recover from any perturbation and re-establish contact with the granular surroundings, and enduring frictional contacts are the primary means of force transmission. If $l_v \gg 1$ the particles lose contact with their neighbors, the granular mixture is disassociated, and particle interactions are primarily collisional; the multiphase mixture becomes a dilute granular flow. The Viscous number ignores numerous microphysical processes such as pore pressure and fluid transport through the adjacent granular media, dissipation associated with lubrication, non-spherical particle shape, non-ideal point contacts (with non-zero surface area), etc.

The granular state of the system at one time step is shown in Fig. 3, which represents the same time step as in Fig. 2e and f. The location of the mixing bowl is

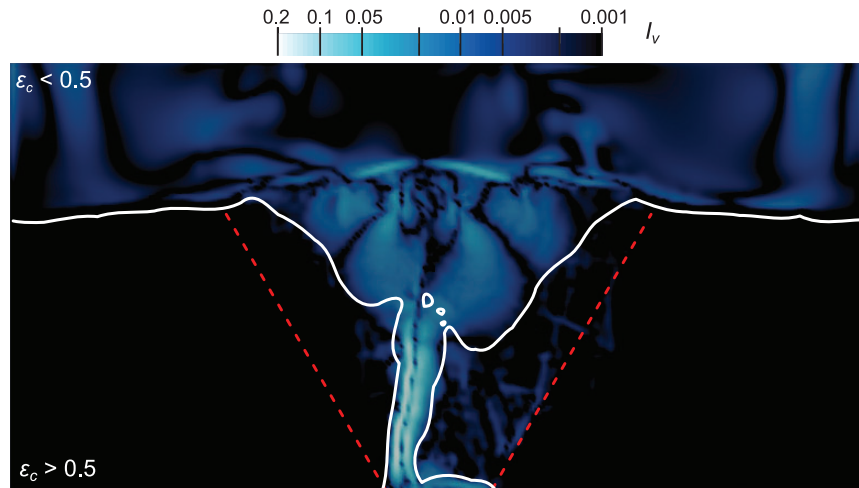


Fig. 3. The Viscous number of the intrusion at $t^* = 1.48$ (Fig. 2e and f). Red dashed lines show the mixing bowl and white lines represent equal volume fractions of liquid and crystals ($\varepsilon_c = \varepsilon_l = 0.5$). l_v is illustrated by shades of blue, represented with a logarithmic scale.

outlined by red dashed lines. The background image illustrates the magnitude of the Viscous number on a logarithmic scale. The white lines represent equal volume fractions of fluid and particles ($\varepsilon_c = 0.5$). In general, $\varepsilon_c > 0.5$ on either side of the contour within the mush, and $\varepsilon_c < 0.5$ in the chimney, fluidized region, and crystal-free portion at the top. An exact value for $\varepsilon_{c,c}$ has not been determined for our system, but the naturally settled bed of monodisperse crystals has an average particle fraction of 0.58, within the critical range for the transition found by Ness & Sun (2015) (polydisperse crystals with respect to size and shape will have a different average packing). Many of the crystals are in pockets of hexagonal packing, but variations from the initial random settling create thin regions of lower particle fractions (Fig. 2b). These thin regions might represent volume fractions less than ε_c , but the dominant behavior of the mush outside the mixing bowl is quasi-static, so we choose to illustrate a particle fraction of 0.5. The regions with the highest values of l_v also have particle fractions of 0.1 or less, corresponding to the dilute granular regime. Regions of the system with higher values of l_v vary through time as liquid in the chimney rises in pulses and meanders through the mixing bowl.

The coordination number, Z , is a measure of the availability of a particle to transmit and dissipate energy by collisional and frictional interactions. The porosity shown in Fig. 2 is a cell-averaged property and is not a complete description of the local granular state of the system. Figure 4 shows the average coordination number as a function of scaled time, with $t^* = (U_0/H_0)t$ for the simulation (Supplementary Data Movie 2). Three distinct phases can be seen that correspond to the three stages described above: a transient start-up period where progressive fluidization produces dilation and a reduction in the coordination number, a quasi steady phase where the dissipation fluctuates around an average indicating both hydrodynamic and granular modes

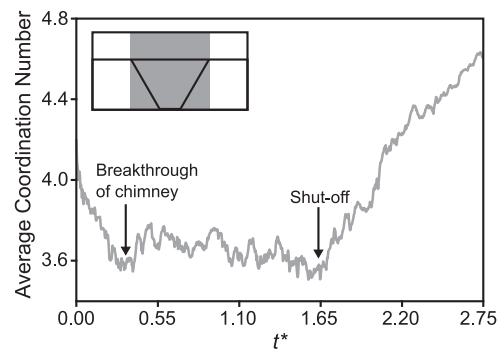


Fig. 4. Average coordination number for crystals within the lateral extent of the mixing bowl (shown as grey box in the inset image) through time. The maximum coordination number for the monodisperse crystals is six, representing hexagonal packing. Also labeled are the times when the crystal-poor chimney breaks through the top of the crystal mush, and the timing of the end of the intrusion when the melt supply is shut off.

of dissipation, and the re-establishment of the granular state once the intrusion ceases. It should be noted that during the collapse of the mixing bowl after the shut-off, the coordination number increases over the original value of the settled bed, reflecting the sensitivity to packing from settling to the proximity of other crystals. Lastly, Fig. 4 shows that the coordination number has a high-frequency component overprinting the long-wavelength temporal behavior. Although our sampling density is not sufficient to do a spectral analysis, we suggest that the high-frequency component may reflect the stochastic ‘chatter’ produced by force chains forming and dissipating as a result of the unsteadiness in the driving fluid flow. Hence it provides a window into the microscale mechanics that recovers a time dependence not apparent in the velocity for example.

Previously, multiphase models for magma dynamics have employed a model for multiphase flow that is an

extension of continuum models. Hence it might seem reasonable to represent the dynamics of the open-system event as a reduced system by invoking either a granular-fluid constitutive model (Boyer *et al.*, 2011) or a mixture continuum rheology with a suspension viscosity. However, Fig. 3 illustrates the challenges in trying to describe the dynamics in those contexts. The shear rate varies in time and space and a local pressure, as required by the model of Boyer *et al.* (2011), is not uniquely defined. Even in regions with low values of I_v , there is still local phase-relative motion and mixing (Schleicher *et al.*, 2016). Extending the granular rheology approach to a non-local constitutive model (Kamrin & Koval, 2012) still requires an assumption of locally steady conditions, which are not obtained in our results, nor likely to be found in nature. Comparisons between our discrete element method (DEM) results and a continuum model for the same system (not shown here) with a yield strength and suspension rheology did not recover the same kinematic template as the higher resolution DEM model, and produced results that were significantly different in the distribution of strain, mixing and particle transport. This exposes the limitations of the suspension rheology approach in high-particle fraction systems and reaffirms the importance of resolving the micro-granular mechanics to adequately address the mechanics of crystal-rich magma mushes.

THE CRYSTAL RECORD OF THE OPEN-SYSTEM EVENT

Much of the evidence for open-system magmatic events comes from processes recorded at the crystal scale, such as zoned crystals and the existence of diverse crystal populations (Wallace & Bergantz, 2002; Costa *et al.*, 2010; Kahl *et al.*, 2011, 2013; Viccaro *et al.*, 2016). When crystals encounter magmatic environments of changing chemical potential, they can respond by growth, recording the changes through chemical zoning, or by dissolution, producing resorption features in the crystals. Open-system mixing can also bring together distinct crystal populations formed by crystals with different reaction histories.

Our particle-based simulations allow us to track crystals and the liquid in which they reside during the open-system intrusion. This capability recovers the crystal gathering and dispersal dynamics. To illustrate crystal transport and reaction during an open-system event, we monitored three pairs of crystals that are proximal at the final time step of the simulation (Fig. 5; Supplementary Data Movie 3). These pairs represent crystals that would be adjacent in a thin section of a volcanic or plutonic sample. Figure 5a shows the trajectories of the three pairs of crystals throughout the simulation. White circles outlined in black indicate the initial locations of each crystal, and black circles outlined in white show the final position of the three crystal pairs. The grey band at the bottom illustrates the

location of the intrusion, and white dotted lines represent the mixing bowl. The image in the background is the final time step of the simulation, showing the mixing between the resident (black) and intruded (white) melts.

Monitoring the three pairs of crystals also illustrates the potential diversity in liquid composition a crystal could encounter during an open-system event (Fig. 5b). The changing liquid composition is associated with a liquid scalar, which represents variations in temperature or chemical composition between the incoming and resident magmas. The liquids in our simulation have been shown to have negligible changes in thermophysical properties, but maintain their compositional distinctions and potential for reaction, so the scalar simply expresses the proportions of intruding and resident liquids with values between zero and one: zero is the resident liquid (black), one is the intruding liquid (white), and values between zero and one are a mixture of the two liquids. Mixing takes place by both advection and chemical diffusion, and the diffusion equation is described in the Supplementary Data. The horizontal axis is the non-dimensionalized time of the simulation, with $t^* = (U_0/H_0)t$. The arrow at $t^* = 1.65$ indicates the end of the intrusion.

The differences in the scalar concentrations encountered by the three pairs of crystals reflect the sensitivity to initial position and the kinematics of subsequent mixing. The purple crystals are initially directly above the intrusion, and are carried up through the mixing bowl by the fingering instabilities that eventually form the crystal-poor chimney. This is the only period of time when they encounter the intruding liquid. Once they reach the top of the mixing bowl, the purple crystals are deposited into the quasi-static edges of the mixing bowl, where little crystal-crystal and crystal-liquid relative motion occurs for the duration of the intrusion and resettling. The green crystals are initially on the edges of the mixing bowl, where the crystal-liquid faults form. Both crystals' motions roughly parallel the faults, first moving upwards as the mush expands to accommodate the intruding liquid, and then downwards as crystals slide down the faults to replace the central crystals entrained by the chimney. The green crystals encounter the chimney liquid only near the end of the intrusion, and approach a mixed scalar concentration of ~ 0.4 as the crystals settle back into the mixing bowl.

The orange crystals encounter a greater diversity of granular regimes than the purple and green pairs. The dark orange crystal initially encounters the intruding liquid, but is left at the base when the instability that carries it merges into the central chimney. Eventually it is entrained in the chimney, but its trajectory is not straight owing to the varicose instabilities of the rising liquid. During this time, the light orange crystal remains in the quasi-static regime, traveling downwards through the mixing bowl until the chimney entrains it as well. Both orange crystals enter the dense, granular vortices, where they travel through the upper portion of the

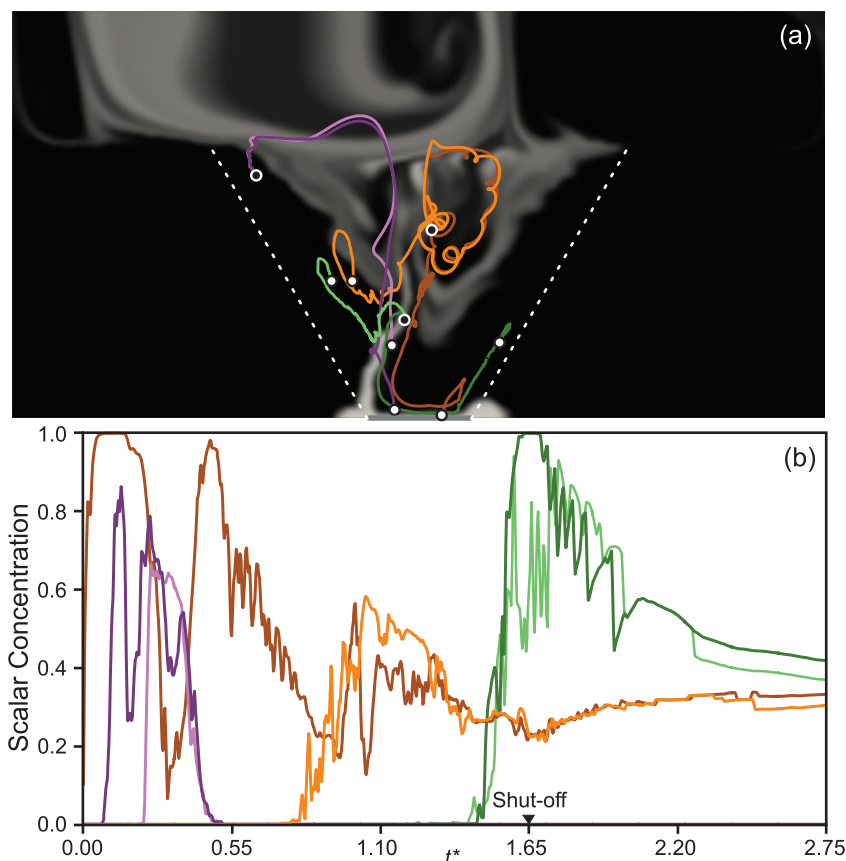


Fig. 5. (a) Trajectories of three pairs of crystals monitored during the simulation. White circles with black outlines illustrate starting location for all crystals; black circles with white outlines show the ending location of each crystal pair. White dashed lines show the mixing bowl. Resident (black) and intruding (white) liquids during the final time of the simulation are shown in the background. (b) The composition of the liquid scalar in which each of the crystals reside. Resident liquid has a scalar concentration of zero; intruding liquid has a value of one. The arrow at $t^* = 1.65$ shows the end of the intrusion.

mixing bowl together, experiencing a full rotation. The dilute and dense regimes of the mixing bowl in this region promote crystal–crystal–liquid mixing, giving a final scalar concentration of ~ 0.3 for the orange crystals. This value is lower than that for the green crystals residing near the fossil chimney liquid, which did not mix as thoroughly with the resident liquid.

We can use the variable scalar compositions encountered by the different crystals to determine what the crystals could record during the single open-system intrusion. We use the approach of [Chen & Zhang \(2008\)](#) [based on the work of [Kerr \(1995\)](#)] to calculate the convective reaction rate of two crystals as they encounter the intruding liquid during the simulation. As a crystal moves through a liquid with changing physicochemical conditions, a compositional boundary layer forms around the crystal. In convective reaction, the relative velocities of the crystal and liquid determine the thickness of the boundary layer, rather than a time-dependent boundary layer in the case of diffusion-controlled dissolution ([Donaldson, 1985](#)). Within the boundary layer, crystal reaction is controlled by the difference in timescales of diffusive mass transfer and interface reaction ([Chen & Zhang, 2008](#)). Although this

model of reaction is most simply described as dissolution, it can also be applied to crystal growth. However, crystal growth is complicated by the possibility of simultaneous growth on existing crystals and the nucleation of new crystals, which would produce different crystal size distributions and clustering ([Špillar & Dolejš, 2013, 2014](#)). Should the reaction rate be negative (indicating growth), it is assumed growth occurs only on pre-existing crystals.

To determine the olivine reaction rate, we use the MgO concentration in the crystals and liquid for the equilibrium-determining component as in [Chen & Zhang \(2008\)](#). We use the MELTS software ([Gualda *et al.*, 2012](#)) to calculate the equilibrium MgO weight per cent in olivine crystals and basaltic liquid at a temperature 50°C colder than the liquidus, with the basalt starting composition from [Rhodes \(1995\)](#). The resident liquid and crystals are assumed to initially be at this lower temperature, and the intruding liquid is at the liquidus temperature. We use a constant density for the liquids, which have nearly equal densities over the temperature range considered; the difference is only 0.6%. Numerical simulations with heat transfer (not shown) indicate that there is little thermal inertia or thermal–chemical

decoupling, so we use the scalar value tracking the intruding liquid as a proxy for the temperature of the liquid. We calculate the temperature using a linear relationship between the scalar concentration and temperature; a scalar value of zero has the temperature of the resident liquid, whereas a value of one represents the liquidus temperature. The results from MELTS provide a linear relationship between temperature and MgO composition, and we use this relationship to estimate the far-field liquid composition in which the crystals reside at every time step.

The convective reaction rate was given by [Chen & Zhang \(2008\)](#) as

$$u = \frac{\beta D}{\delta} \quad (5)$$

which comprises the diffusivity (D) of the equilibrium-determining component (here MgO) and the compositional boundary layer thickness (δ). The boundary layer thickness is determined by the relative velocity between the crystal and the surrounding liquid, and the diffusivity of the equilibrium-determining component (MgO) in the liquid [see equations (7)–(10) of [Chen & Zhang \(2008\)](#)]. The boundary layers calculated in the simulation range between $\sim 10^{-5}$ and 10^{-4} m. Also included in the convective reaction rate is a dimensionless parameter (β) that determines crystal growth or dissolution (negative or positive value, respectively):

$$\beta = \frac{\rho_l(C_0 - C_\infty)}{\rho_c(C_c - C_0)} \quad (6)$$

This parameter depends on the densities of the liquid (ρ_l) and crystal (ρ_c), the MgO weight per cent in the liquid within the crystal–liquid interface (C_0), the far-field (i.e. the liquid computational cell) MgO weight per cent (C_∞), and the MgO weight per cent in the crystal (C_c). We use the thermometer of [Putirka \[2008, equation \(13\)\]](#) to calculate the interface liquid composition as a function of temperature (T), which is independent of

pressure and the compositions of the far-field melt and crystal:

$$C_0 = \frac{T - 994.4}{26.3} \quad (7)$$

To apply this approach to our simulation, we assumed the crystals were initially in equilibrium with the resident liquid (i.e. $C_0 = C_\infty$). However, the interface melt composition is independent of the composition of the crystals and the external melt [equation (7)], and because of this produces disequilibrium conditions when the crystals are stationary within the resident melt. The reaction rate calculation [equation (5)] is for convective reaction, therefore stationary crystals require a convection-free model that is beyond the scope of this study ([Liang, 2000; Chen & Zhang, 2008](#)). We apply the calculation only to crystals that are continuously moving relative to the liquid (the orange crystals from [Fig. 5](#)). The light orange crystal does not encounter the intruding liquid during the beginning of the intrusion, so we set the crystal dissolution rate to zero during this time.

The results of the reaction calculation for the two orange crystals are shown in [Fig. 6](#). Both crystals experience positive reaction rates, indicating that they undergo dissolution only when interacting with the intruding liquid. During the simulation, the dark orange crystal would dissolve a total of $0.38 \mu\text{m}$ from the rim, whereas the light orange crystal, which encountered the intruding liquid later in the simulation, would dissolve $0.25 \mu\text{m}$. The high-frequency variations in the crystals' dissolution rates are due to the changing scalar concentration (see [Fig. 5b](#)) and relative velocity between each crystal and the surrounding liquid. Despite being highly variable, the relative velocities are low, with Reynolds numbers between $\sim 10^{-4}$ and one. The average rates of dissolution for the examined crystals are $13.7 \mu\text{m h}^{-1}$ for the dark orange crystal, and $12.6 \mu\text{m h}^{-1}$ for the light orange crystal during the time it encountered the intruding liquid. Assuming constant

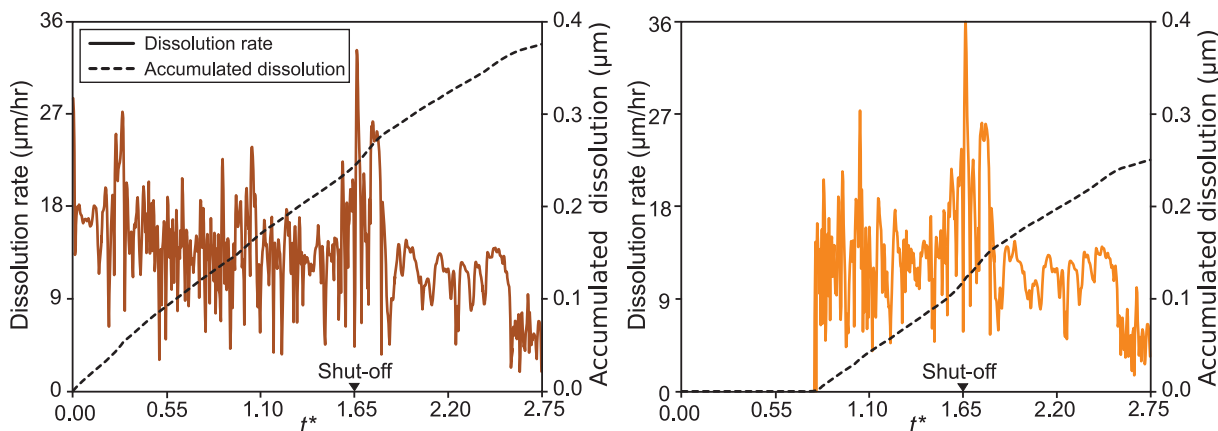


Fig. 6. Dissolution experienced by the orange crystals from [Fig. 5](#). Continuous light and dark orange lines show the dissolution rate that each crystal experiences during the simulation. Dashed black lines show the accumulated dissolution rate that both crystals experience during the simulation. The arrow at $t^* = 1.65$ shows the end of the intrusion.

dissolution rates with these averages, the 2 mm radius crystals would dissolve fully after $\sim 6\text{--}7$ days.

The convective reaction rates calculated from the simulation fall within the range of rates from previous experiments and theoretical calculations for similar temperatures and compositions. Experiments by Donaldson (1985) gave dissolution rates for olivine at near-liquidus temperatures of $9\text{--}14\ \mu\text{m h}^{-1}$. Liang (2000) calculated theoretical rates for olivine solid solution diffusion-controlled (rather than convection-controlled) dissolution of $\sim 3\text{--}36\ \mu\text{m h}^{-1}$. The rates we calculate are lower than the hypothetical dissolution rate of $52.6\ \mu\text{m h}^{-1}$ calculated by Chen & Zhang (2008), who considered a crystal falling in a melt with a constant, disequilibrium composition. The crystal and liquid compositions chosen for the example used by Chen & Zhang (2008) represent a larger disequilibrium than the compositions in this study, which explains the faster dissolution rates. We conclude that the rates calculated for the crystals represent realistic values when reacting by convective dissolution to the intruding liquid.

The reaction rates for the orange pair of crystals represent crystal dissolution when they encounter the intruding liquid. However, natural crystals can have reversely zoned rims, indicating that the rims grew from a more primitive liquid prior to eruption. For crystal growth to occur in our simulation, the far-field composition of the melt (C_∞) would need a higher MgO content than that of the interface liquid (C_0). These quantities are both calculated as functions of temperature [from MELTS and equation (7)], and for a given temperature C_0 is always greater than C_∞ . In the presented simulations, the crystal, interface liquid, and far-field liquid are at the same temperature, making crystal growth impossible. However, if the thermal inertia of a crystal were considered, it is possible for a crystal encountering a higher temperature far-field liquid to generate a thermal (and therefore, compositional) gradient that would promote crystal growth. This hypothesis requires additional simulations that include heat transfer to monitor the temperatures of the crystals and far-field liquid separately.

GEOLOGICAL IMPLICATIONS OF THE OPEN-SYSTEM MODEL

Although our DEM-CFD model of intrusion of a melt into an olivine mush is highly simplified, we offer some tentative implications of the modeling that may illuminate conditions found in natural examples. The primary benefits of using DEM-CFD arise from the resolution of small-scale crystal–crystal mechanical interactions, and the tracking of individual crystal trajectories and response as mixing proceeds.

The resolution of crystal-scale interactions allows for extreme strain localization and frictional behavior to be modeled. It is this behavior that produces the distinct morphology of the mixing bowl. And similar processes operating in a mush may produce the frequent

observation of cryptic internal contacts in plutons, which are often rootless in the sense that they do not obviously connect with any through-going externally derived tectonic feature. Rather, these features juxtapose elements of a crystal-mush with itself, producing cross-cutting looking features but without substantial changes in mode (Paterson, 2009). Hence any external or internal process that can produce pressure changes such that some fluidization can locally occur, releasing frictional crystal contacts, may produce what is recognized in the field as a contact. That contact itself may not have any significance in the sense of magmas that are temporally discordant and originate elsewhere. The simulations suggest that in hydrogranular systems such as a crystal mush, frictional forces are to be expected and strain localization is common. Hence models that invoke a continuum assumption to describe geological observations are not adequate for crystal-rich systems, perhaps to even as low as 30% crystallinity, and describing crystal-rich transport with notions taken from simple fluid dynamics as done by Glazner (2014), are inadequate to illuminate the diversity of behavior encountered in natural examples.

Another feature of the mixing process described above [also see Schleicher *et al.* (2016)] is that new magma injections interact with the mushy reservoir in a pulsating fashion. The fact that enclaves are very common in silicic rocks but their feeder systems are rarely recognized suggests that the production of discrete enclaves and the ‘digestion’ or break-up of their feeder system happen simultaneously. As seen in Fig. 2, the pulsating mechanical response of the mush bifurcates the incoming magma. If the host magma was silicic and the incoming magma mafic and subject to chilling to produce a stable but ductile rind, this process would produce enclaves, and erase the distinct dike-like character of the feeder zone as suggested in Fig. 2g.

The simulations of crystal chemical response to open-system input, although highly simplified, make it clear that caution is warranted when using the crystal record of open-system events to infer distinct mixing episodes; the interested reader is directed to Schleicher *et al.* (2016) for more discussion of mixing systematics. Although we consider only a few crystals here as proof of concept examples, even in this highly simplified scenario the crystal cargo is incredibly diverse. And although we are not in a position yet to offer quantitative statistical guidelines to address sample ergodicity in resolving distinct open-system events, it is to be expected that proximal crystals will probably have discordant reaction time-series.

CONCLUSIONS

The presented simulation illustrates the localized response of a crystal-rich mush to an open-system intrusion. The emergence of the fluidized mixing bowl confines crystal and liquid mixing to this region, whereas the surrounding mush is relatively unaffected.

Little to no intruded liquid passes through the mush into the overlying reservoir without some mixing with the resident liquid owing to vertical transport and overturn in the mixing bowl. The self-similarity of the mixing bowl indicates that different intrusion rates or mush characteristics (e.g. liquid and crystal composition, mush height, intrusion width) would generate a similar fluidized region, as long as the intruding liquid exceeds the minimum fluidization velocity of the mush. Prolonged intrusion could increase the lateral extent of the mixing bowl as crystals erode along the crystal–liquid faults, but the overall geometry would persist.

Although the simulation represents a geologically simple system, we document the mechanical and compositional diversity that can arise from an open-system intrusion. The mixing bowl and surrounding mush contain a variety of hydrogranular regimes, reflecting the changes in local crystal fraction and coordination number. The variation in these regimes leads to non-affine crystal and liquid motion within the mixing bowl. Crystals that are proximal at the end of the intrusion may have followed different trajectories through the mixing bowl and reacted with a variety of liquid compositions. Whereas the tracked crystals in our simulation undergo only dissolution when reacting with the intruding liquid, natural systems with variable liquid temperatures and compositions could produce a complex crystal cargo, even from a single open-system event.

ACKNOWLEDGEMENTS

We are grateful to Keith Putirka for helpful comments regarding the olivine thermometer, and to Matthias Hort, Fidel Costa and an anonymous reviewer for comments that improved the quality and clarity of this paper. We also acknowledge the important role played by editor Jim Beard, whose helpful comments and support reflect the professionalism of the *Journal of Petrology*. We also thank the developers at the National Energy and Technology Lab for assistance modifying their code; the open-source software, MFIX, used to create the simulation is available at <https://mfix.netl.doe.gov/>.

SUPPLEMENTARY DATA

Supplementary data for this paper are available at *Journal of Petrology* online.

FUNDING

This work was supported by the National Science Foundation (DGE-1256082, EAR-1049884, EAR-1447266) and access to computational facilities was supported by the National Science Foundation-funded Extreme Science and Engineering Discovery Environment consortium (TG-EAR140013).

REFERENCES

- Andreotti, B., Forterre, Y. & Pouliquen, O. (2013). *Granular Media: Between Fluid and Solid*. Cambridge: Cambridge University Press.
- Baker, S. & Amelung, F. (2012). Top-down inflation and deflation at the summit of Kilauea Volcano, Hawai'i observed with InSAR. *Journal of Geophysical Research (Solid Earth)* **117**, B12406.
- Bergantz, G. W. & Breidenthal, R. E. (2001). Non-stationary entrainment and tunneling eruptions: A dynamic link between eruption processes and magma mixing. *Geophysical Research Letters* **28**, 3075–3078.
- Bergantz, G. W., Schleicher, J. M. & Burgisser, A. (2015). Open-system dynamics and mixing in magma mushes. *Nature Geoscience* **8**, 793–796.
- Boyer, F., Guazzelli, E. & Pouliquen, O. (2011). Unifying suspension and granular rheology. *Physical Review Letters* **107**, 188301.
- Burgisser, A. & Bergantz, G. W. (2011). A rapid mechanism to remobilize and homogenize highly crystalline magma bodies. *Nature* **471**, 212–215.
- Burgisser, A., Bergantz, G. W. & Breidenthal, R. E. (2005). Addressing complexity in laboratory experiments: The scaling of dilute multiphase flows in magmatic systems. *Journal of Volcanology and Geothermal Research* **141**, 245–265.
- Cassar, C., Nicolas, M. & Pouliquen, O. (2005). Submarine granular flows down inclined planes. *Physics of Fluids (1994–present)* **17**, 103301.
- Cates, M. E., Wittmer, J. P., Bouchaud, J.-P. & Claudin, P. (1998). Jamming, force chains, and fragile matter. *Physical Review Letters* **81**, 1841–1844.
- Chen, Y. & Zhang, Y. (2008). Olivine dissolution in basaltic melt. *Geochimica et Cosmochimica Acta* **72**, 4756–4777.
- Cooper, K. M. (2015). Timescales of crustal magma reservoir processes: insights from U-series crystal ages. In: Caricchi, L. & Blundy, J. D. (eds) *Chemical, Physical and Temporal Evolution of Magmatic Systems*. Geological Society, London, *Special Publications* **422**, 141–174.
- Cooper, K. M., Sims, K. W. W., Eiler, J. M. & Banerjee, N. (2016). Timescales of storage and recycling of crystal mush at Krafla Volcano, Iceland. *Contributions to Mineralogy and Petrology* **171**, 1–19.
- Costa, F. & Morgan, D. (2011). Time constraints from chemical equilibrium in magmatic crystals. In: Dosseto, A., Turner, S. & Van-Orman, J. (eds) *Timescales of Magmatic Processes*. Chichester: John Wiley, pp. 125–159.
- Costa, F., Coogan, L. A. & Chakraborty, S. (2010). The time scales of magma mixing and mingling involving primitive melts and melt–mush interaction at mid-ocean ridges. *Contributions to Mineralogy and Petrology* **159**, 371–387.
- Cui, X., Li, J., Chan, A. & Chapman, D. (2014). Coupled DEM–LBM simulation of internal fluidisation induced by a leaking pipe. *Powder Technology* **254**, 299–306.
- da Cruz, F., Emam, S., Prochnow, M., Roux, J.-N. & Chevoir, F. (2005). Rheophysics of dense granular materials: Discrete simulation of plane shear flows. *Physical Review E* **72**, 21309.
- Daerr, A. & Douady, S. (1999). Sensitivity of granular surface flows to preparation. *EPL (Europhysics Letters)* **47**, 324.
- Donaldson, C. H. (1985). The rates of dissolution of olivine, plagioclase, and quartz in a basalt melt. *Mineralogical Magazine* **49**, 683–693.
- du Pont, S. C., Gondret, P., Perrin, B. & Rabaud, M. (2003). Granular avalanches in fluids. *Physical Review Letters* **90**, 44301.
- Ergun, S. (1952). Fluid flow through packed columns. *Chemical Engineering Progress* **48**, 89–94.

- Estep, J. & Dufek, J. (2012). Substrate effects from force chain dynamics in dense granular flows. *Journal of Geophysical Research: Earth Surface* **117**, F01028.
- Geist, D. J., Fornari, D. J., Kurz, M. D., Harpp, K. S., Soule, S. A., Perfit, M. R. & Koleszar, A. M. (2006). Submarine Fernandina: Magmatism at the leading edge of the Galápagos hot spot. *Geochemistry, Geophysics, Geosystems* **7**, Q12007.
- Gerbi, C., Johnson, S. E. & Paterson, S. R. (2004). Implications of rapid, dike-fed pluton growth for host-rock strain rates and emplacement mechanisms. *Journal of Structural Geology* **26**, 583–594.
- Girard, G. & Stix, J. (2009). Buoyant replenishment in silicic magma reservoirs: Experimental approach and implications for magma dynamics, crystal mush remobilization, and eruption. *Journal of Geophysical Research: Solid Earth* **114**, B08203.
- Glazner, A. F. (2014). Magmatic life at low Reynolds number. *Geology* **42**, 935–938.
- Goldhirsch, I. (2003). Rapid granular flows. *Annual Review of Fluid Mechanics* **35**, 267–293.
- Gualda, G. A. R., Ghiorsso, M. S., Lemons, R. V. & Carley, T. L. (2012). Rhyolite-MELTS: a modified calibration of MELTS optimized for silica-rich, fluid-bearing magmatic systems. *Journal of Petrology* **53**, 875–890.
- Huber, C., Bachmann, O. & Dufek, J. (2012). Crystal-poor versus crystal-rich ignimbrites: A competition between stirring and reactivation. *Geology* **40**, 115–118.
- Huppert, H. E., Sparks, R. S. J., Whitehead, J. A. & Hallworth, M. A. (1986). Replenishment of magma chambers by light inputs. *Journal of Geophysical Research: Solid Earth* **91**, 6113–6122.
- Jaeger, H. M., Nagel, S. R. & Behringer, R. P. (1996). Granular solids, liquids, and gases. *Reviews of Modern Physics* **68**, 1259–1273.
- Johnsen, Ø., Chevalier, C., Lindner, A., Toussaint, R., Clément, E., Måløy, K. J., Flekkøy, E. G. & Schmittbuhl, J. (2008). Decompaction and fluidization of a saturated and confined granular medium by injection of a viscous liquid or gas. *Physical Review E* **78**, 51302.
- Johnson, D. J., Eggert, A. A., Bagnardi, M., Battaglia, M., Poland, M. P. & Miklius, A. (2010). Shallow magma accumulation at Kilauea Volcano, Hawai'i, revealed by microgravity surveys. *Geology* **38**, 1139–1142.
- Jop, P. (2015). Rheological properties of dense granular flows. *Comptes Rendus Physique* **16**, 62–72.
- Kahl, M., Chakraborty, S., Costa, F. & Pompilio, M. (2011). Dynamic plumbing system beneath volcanoes revealed by kinetic modeling, and the connection to monitoring data: An example from Mt. Etna. *Earth and Planetary Science Letters* **308**, 11–22.
- Kahl, M., Chakraborty, S., Costa, F., Pompilio, M., Liuzzo, M. & Viccaro, M. (2013). Compositionally zoned crystals and real-time degassing data reveal changes in magma transfer dynamics during the 2006 summit eruptive episodes of Mt. Etna. *Bulletin of Volcanology* **75**, 1–14.
- Kamrin, K. & Koval, G. (2012). Nonlocal constitutive relation for steady granular flow. *Physical Review Letters* **108**, 178301.
- Kerr, R. C. (1995). Convective crystal dissolution. *Contributions to Mineralogy and Petrology* **121**, 237–246.
- Liang, Y. (2000). Dissolution in molten silicates: effects of solid solution. *Geochimica et Cosmochimica Acta* **64**, 1617–1627.
- Marsh, B. D. (1981). On the crystallinity, probability of occurrence, and rheology of lava and magma. *Contributions to Mineralogy and Petrology* **78**, 85–98.
- MiDi, G. D. R. (2004). On dense granular flows. *European Physical Journal E* **14**, 341–365.
- Moore, A., Coogan, L. A., Costa, F. & Perfit, M. R. (2014). Primitive melt replenishment and crystal-mush disaggregation in the weeks preceding the 2005–2006 eruption, 9°50'N, EPR. *Earth and Planetary Science Letters* **403**, 15–26.
- Neave, D. A., Passmore, E., Maclennan, J., Fitton, G. & Thordarson, T. (2013). Crystal–melt relationships and the record of deep mixing and crystallization in the AD 1783 Laki eruption, Iceland. *Journal of Petrology* **54**, 1661–1690.
- Ness, C. & Sun, J. (2015). Flow regime transitions in dense non-Brownian suspensions: Rheology, microstructural characterization, and constitutive modeling. *Physical Review E* **91**, 12201.
- Ness, C. & Sun, J. (2016). Two-scale evolution during shear reversal in dense suspensions. *Physical Review E*, **93**, 12604.
- Passmore, E., Maclennan, J., Fitton, G. & Thordarson, T. (2012). Mush disaggregation in basaltic magma chambers: Evidence from the AD 1783 Laki eruption. *Journal of Petrology* **53**, 2593–2623.
- Paterson, S. R. (2009). Magmatic tubes, pipes, troughs, diapirs, and plumes: Late-stage convective instabilities resulting in compositional diversity and permeable networks in crystal-rich magmas of the Tuolumne batholith, Sierra Nevada, California. *Geosphere* **5**, 496–527.
- Perugini, D. & Poli, G. (2005). Viscous fingering during replenishment of felsic magma chambers by continuous inputs of mafic magmas: Field evidence and fluid-mechanics experiments. *Geology* **33**, 5–8.
- Peters, I. R., Majumdar, S. & Jaeger, H. M. (2016). Direct observation of dynamic shear jamming in dense suspensions. *Nature* **532**, 214–217.
- Philippe, P. & Badiane, M. (2013). Localized fluidization in a granular medium. *Physical Review E* **87**, 42206.
- Philpotts, A. R., Brustman, C. M., Shi, J., Carlson, W. D. & Denison, C. (1999). Plagioclase-chain networks in slowly cooled basaltic magma. *American Mineralogist* **84**, 1819–1829.
- Putirka, K. D. (2008). Thermometers and barometers for volcanic systems. In: Putirka, K. D. & Tepley, F. J., III (eds) *Minerals, Inclusions and Volcanic Processes. Mineralogical Society of America and Geochemical Society, Reviews in Mineralogy and Geochemistry* **69**, 61–120.
- Reid, M. R. (2008). How long does it take to supersize an eruption? *Elements* **4**, 23–28.
- Rhodes, J. M. (1988). Geochemistry of the 1984 Mauna Loa Eruption: Implications for magma storage and supply. *Journal of Geophysical Research: Solid Earth* **93**, 4453–4466.
- Rhodes, J. M. (1995). The 1852 and 1868 Mauna Loa picrite eruptions: clues to parental magma compositions and the magmatic plumbing system. In: Rhodes, J. M. & Lockwood, J. P. (eds) *Mauna Loa Revealed: Structure, Composition, History, and Hazards. American Geophysical Union, Geophysical Monograph* **92**, 241–262.
- Roux, J.-N. (2009). The nature of quasistatic deformation in granular materials. In: García-Rojo, R., Herrmann, H. J. & McNamara, S. (eds) *Powders and Grains, Proceedings of the 5th International Conference on Micromechanics of Granular Media, Stuttgart, Germany, 18–22 July 2005*. Leiden: Balkema, pp. 261–265.
- Ruprecht, P., Bergantz, G. W. & Dufek, J. (2008). Modeling of gas-driven magmatic overturn: Tracking of phenocryst dispersal and gathering during magma mixing. *Geochemistry, Geophysics, Geosystems* **9**, Q07017.
- Sandnes, B., Flekkøy, E. G., Knudsen, H. A., Måløy, K. J. & See, H. (2011). Patterns and flow in frictional fluid dynamics. *Nature Communications* **2**, 288.

- Schleicher, J. M., Bergantz, G. W., Breidenthal, R. E. & Burgisser, A. (2016). Time scales of crystal mixing in magma mushes. *Geophysical Research Letters* **43**, 1543–1550.
- Schmitt, A. K. (2011). Uranium series accessory crystal dating of magmatic processes. *Annual Review of Earth and Planetary Sciences* **39**, 321–349.
- Shea, T., Lynn, K. J. & Garcia, M. O. (2015). Cracking the olivine zoning code: Distinguishing between crystal growth and diffusion. *Geology* **43**, 935–938.
- Špillar, V. & Dolejš, D. (2013). Calculation of time-dependent nucleation and growth rates from quantitative textural data: Inversion of crystal size distribution. *Journal of Petrology* **54**, 913–931.
- Špillar, V. & Dolejš, D. (2014). Kinetic model of nucleation and growth in silicate melts: Implications for igneous textures and their quantitative description. *Geochimica et Cosmochimica Acta* **131**, 164–183.
- Streck, M. J. (2008). Mineral textures and zoning as evidence for open system processes. In: Putirka, K. D. & Tepley, F. J., III (eds) *Minerals, Inclusions and Volcanic Processes*. Mineralogical Society of America and Geochemical Society, *Reviews in Mineralogy and Geochemistry* **69**, 595–622.
- Sun, Q., Jin, F., Liu, J. & Zhang, G. (2010). Understanding force chains in dense granular materials. *International Journal of Modern Physics B* **24**, 5743–5759.
- Thomson, A. & MacLennan, J. (2013). The distribution of olivine compositions in Icelandic basalts and picrites. *Journal of Petrology* **54**, 745–768.
- Trulsson, M., Andreotti, B. & Claudin, P. (2012). Transition from the viscous to inertial regime in dense suspensions. *Physical Review Letters* **109**, 118305.
- Viccaro, M., Giuffrida, M., Nicotra, E. & Cristofolini, R. (2016). Timescales of magma storage and migration recorded by olivine crystals in basalts of the March–April 2010 eruption at Eyjafjallajökull volcano, Iceland. *American Mineralogist* **101**, 222–230.
- Wallace, G. S. & Bergantz, G. W. (2002). Wavelet-based correlation (WBC) of zoned crystal populations and magma mixing. *Earth and Planetary Science Letters* **202**, 133–145.
- Wallace, G. S. & Bergantz, G. W. (2005). Reconciling heterogeneity in crystal zoning data: An application of shared characteristic diagrams at Chaos Crags, Lassen Volcanic Center, California. *Contributions to Mineralogy and Petrology* **149**, 98–112.

SUPPLEMENTARY TEXT

The mechanics and temporal evolution of an open-system magmatic intrusion into a crystal-rich magma

J. M. Schleicher¹, G. W. Bergantz¹

¹Department of Earth and Space Sciences, University of Washington, Seattle, Washington, 98195 USA

INTRODUCTION

This supplementary text includes details of three supplementary movie files. It also provides details of the simulation methods, which include the model theory and governing equations, simulation initialization, and code validation.

SUPPLEMENTARY MOVIES

Movie 1

Movie of Figure 2, showing the simulation of the open-system intrusion into the crystal-rich mush. The left shows the crystals and liquids, and the right shows the corresponding crystal volume fraction.

Movie 2

The same simulated intrusion as Movie S1, but the crystals are colored based on their coordination number. Values range from one, representing crystals touching only one other crystal, to six where crystals are in hexagonal packing. Figure 4 shows the average coordination number of crystals within the indicated region (see Figure 4 inset) through time, calculated from this movie.

Movie 3

The same simulation as Movies 1 and 2, highlighting the crystals monitored in Figures 5 and 6. The three pairs of crystals have been shown with the same colors in these figures, but are 2.5 times larger than their actual size to increase their visibility.

SIMULATION METHODS

Multiphase fluid simulation theory and algorithm

We performed simulations using a modified version of the MFIx (Multiphase Flow with Interphase eXchange) numerical algorithm developed by the DoE supported National Energy and Technology Laboratory. It simulates multiphase flow by employing discrete element method-computational fluid dynamics (DEM-CFD). This is a Lagrangian-Eulerian approach for solid (crystal) and fluid (liquid) phases, respectively, where crystal phases are explicitly resolved and the liquid phase is treated as a continuum. This method allows us to model hydrodynamic, hydrodynamic-to-crystal, crystal-to-hydrodynamic and crystal-to-crystal interactions, that is, the so-called 4-way coupling. Collisions, sustained frictional contact, buoyancy, fluid drag and interphase momentum transport between phases are directly resolved with the soft-sphere approach, using a spring-dashpot system to model the contact forces (Cundall & Strack, 1979). The MFIx DEM-CFD algorithm has been verified and validated (Garg *et al.*, 2012a, 2012b; Li *et al.*, 2012) including the physical effects of chemical reactions (Li & Guenther, 2012); validation is discussed in detail below. Our simulations were run on the Stampede Cluster at the Texas Advanced Computing Center (TACC).

Governing Equations

The liquid phase is described with the governing equations for mass and momentum conservation:

$$\frac{\partial \varepsilon_l \rho_l}{\partial t} + \nabla \cdot (\varepsilon_l \rho_l \mathbf{v}_l) = 0 \quad 1$$

$$\frac{D}{Dt} (\varepsilon_l \rho_l \mathbf{v}_l) = \nabla \cdot \overline{\overline{\mathbf{S}}_l} + \varepsilon_l \rho_l \mathbf{g} - \mathbf{I}_{lc} \quad 2$$

Here, ε_l is the volume fraction of the liquid phase, ρ_l is the liquid density, \mathbf{v}_l is the liquid phase velocity vector, \mathbf{g} is the gravitational acceleration, \mathbf{I}_{lc} is a coupling term that involves the transfer of momentum between the liquid and crystal phases, and $\overline{\overline{\mathbf{S}}_l}$ is the liquid-phase stress-tensor, given by:

$$\overline{\overline{\mathbf{S}}_l} = -P_l \overline{\overline{\mathbf{I}}} + \overline{\overline{\mathbf{t}}_l} \quad 3$$

$$\overline{\overline{\mathbf{t}}_l} = 2\mu_l \overline{\overline{\mathbf{D}}_l} + \lambda_l \text{tr}(\overline{\overline{\mathbf{D}}_l}) \overline{\overline{\mathbf{I}}} \quad 4$$

$$\overline{\overline{\mathbf{D}}_l} = \frac{1}{2} \left[\nabla \mathbf{v}_l + (\nabla \mathbf{v}_l)^\top \right] \quad 5$$

P_l is the liquid-phase pressure, $\overline{\overline{\mathbf{I}}}$ is the identity matrix, and $\overline{\overline{\mathbf{t}}_l}$ is the liquid-phase shear stress tensor. μ_l and λ_l are the dynamic viscosity and second coefficient of viscosity for the liquid phase, and $\overline{\overline{\mathbf{D}}_l}$ is the strain rate tensor. The second coefficient of viscosity is typically small but included here for completeness.

An advection-diffusion equation is employed to model transport of a scalar attached to the liquid phase. This scalar acts as an inert tracer of a compositional field associated with new magma and is shared by mixing between the resident and incoming liquids:

$$\frac{\partial}{\partial t}(\varepsilon_i \rho_l C_l) + \nabla \cdot (\varepsilon_i \rho_l \mathbf{v}_l C_l) = \nabla \cdot (D_l \nabla C_l) \quad 6$$

Here C_l is the concentration of the liquid scalar and D_l is the diffusion coefficient for the scalar in the liquid phase. The cation diffusivity in basaltic melts is typically of order 10^{-10} m²/s (Richter *et al.*, 2003). This produces a scalar Peclet number of at least order 10^5 for the most active regions of flow for the duration of the simulations. Therefore, the scalar diffusivity was set to zero with no noticeable change in the scalar field. Hence modeled variations in the scalar field are entirely due to advective mixing and numerical diffusion. We did not quantify the effects of numerical diffusion on scalar mixing.

The crystals in the simulation are Lagrangian particles, with coupled equations solved for individual crystals at each time step. The position of the crystals and their linear and angular momentum are calculated according to Newton's Laws:

$$\frac{d\mathbf{X}^{(i)}(t)}{dt} = \mathbf{V}^{(i)}(t) \quad 7$$

$$m^{(i)} \frac{d\mathbf{V}^{(i)}(t)}{dt} = \mathbf{F}_T^{(i)}(t) = m^{(i)} \mathbf{g} + \mathbf{F}_d^{(i\hat{l}k)}(t) + \mathbf{F}_c^{(i)}(t) \quad 8$$

$$I^{(i)} \frac{d\boldsymbol{\omega}^{(i)}(t)}{dt} = \mathbf{T}^{(i)}(t) \quad 9$$

The superscript (i) represents each crystal within the domain, $\mathbf{X}^{(i)}(t)$ is the crystal position, $\mathbf{V}^{(i)}(t)$ is the crystal linear velocity, and $m^{(i)}$ is the i^{th} crystal's mass. $\mathbf{F}_T^{(i)}(t)$ is the sum of the forces acting upon the i^{th} crystal, $\mathbf{F}_d^{(i\hat{l}k)}(t)$ is the total drag force on the i^{th} crystal in the k^{th} liquid cell, and $\mathbf{F}_c^{(i)}(t)$ is the contact force from interactions with other

crystals. The equation for angular velocity, $\boldsymbol{\omega}^{(i)}(t)$, includes the i^{th} crystal's moment of inertia $I^{(i)} = \frac{m^{(i)} d_c^{(i)}}{10}$ and the sum of the torques $\mathbf{T}^{(i)}(t)$ acting on the i^{th} crystal.

Additional details of the implementation of the spring-and-dashpot model for calculating collisional forces used in MFIx can be found in the documentation of the MFIx-DEM algorithm (Garg *et al.*, 2012b). The values of the crystal-crystal coefficient of friction, restitution, and spring constant required for DEM are 0.1, 0.1, and 10^5 kg/s², respectively. The sensitivity of model outcomes to the choice of DEM parameters depends on the dynamic regime considered (Paulick *et al.*, 2015) although it has been noted particle dynamics in fluidized beds are not very sensitive to the choice of DEM contact parameters (Tsuji *et al.*, 1993). The coefficients of friction (μ_f) for non-compacted, olivine crystals in melt have never been measured. Hence we assessed the sensitivity of both the quasi-static and fully-fluidized model results to variations in contact friction from values of 0.03 to 0.5. Neither the quasi-static results, the formation of fluidized granular eddies, nor the mixing characteristics changed significantly over this interval, so a value of 0.1 was used.

For brevity we do not repeat the development of the DEM model in-depth where the restitution coefficients and spring constants are defined, the interested reader is directed to Garg *et al.* (2012a, 2012b). The value of the restitution coefficient (e) changes for collisions of particles in a viscous liquid, as shown by experimental results (Yang & Hunt, 2006). The authors defined a parameter called the binary Stokes number for colliding particles in a viscous liquid:

$$St_B = \frac{m^* (U_1 - U_2)}{6\rho m_l (r_c^*)^2} \quad 10$$

where $m^*=(1/m_1+1/m_2)^{-1}$ and $r_c^*=(1/r_1+1/r_2)^{-1}$ are the reduced mass and radius of the two particles in the collision, respectively, (U_1-U_2) is the relative approach velocity of the particles, and μ_l is the fluid dynamic viscosity. The restitution coefficient of two colliding particles increases with increasing St_B . Our simulations generate $St_B \ll 1$, therefore based on the empirical data of particle-particle and particle-wall interaction in a viscous fluid the choice of $e = 0.1$ is appropriate (Yang & Hunt, 2006).

The values used for the particle stiffness coefficients (k_n, k_t) are smaller than those of the natural materials because using the actual values incurs simulation times that exceed any practical limits. However it has been shown in validation studies that reducing the particle stiffness coefficients (spring constants) does not produce measureable error, and this is common practice throughout the CFD-DEM community (Nakamura & Watano, 2007). A DEM study (Coetzee & Els, 2009) demonstrated that particle stiffness coefficients below 10^5 kg/s^2 resulted in variable internal friction angle within the granular material. However, for k_n values at and above 10^5 kg/s^2 and low particle friction coefficients ($\mu_f < 0.2$), the angle of internal friction did not vary as a function of stiffness coefficient. We also performed a sensitivity study of the stiffness coefficients and found values that satisfy validation and do not give unrealistic compaction of the particle bed

Simulation initialization and properties

The simulations are 2.5-D, with the third dimension equaling the width of a crystal. Our simulation is for a dike-like body whose long dimension is into-and-out-of the plane of the domain, so 3-D edge effects are ignored and the liquid motion is governed by the quasi-2-D geometry. Accurate resolution of both the liquid and crystal dynamics requires

that the liquid continuum grid-cell size has to be less than 1/19.3 of the domain size, and larger than 1.63 crystal diameters (Peng *et al.*, 2014). We performed grid resolution studies and found that at a grid cell of 2.5 crystal diameters gave stable and reproducible results. The number of crystals is well above the minimum required to recover scalable, ensemble-averaged behavior (Ness & Sun, 2015).

The injection rate used in the simulation falls within the range of magma ascent rates of 10^{-4} - 10^1 m/s for volcanoes in a range of tectonic settings as estimated by geochemical, petrographic, and geophysical studies (Girard & Stix, 2009; Parks *et al.*, 2012; Rutherford, 2008). Specifying the intrusion rate is appropriate for modeling open-system events driven by momentum, rather than by thermal or compositional buoyancy. This choice of input style is motivated by the common occurrence of a complex crystal cargo in mixed magmas, with crystal clots, rapidly created disequilibrium features, and evidence for near instantaneous mingling of large volumes of magma (Costa *et al.*, 2010; Davidson *et al.*, 2001; Wallace & Bergantz, 2005), all of which indicate that many open-system events are strongly forced and can undergo mixing and mingling. In addition many open-system events have evidence that the open-system process has sufficient energy to overcome viscosity barriers producing mingled magmas with crystal transfer (Ruprecht *et al.*, 2012) as well as evidence of crystals transported out of a crystal mush which requires fluidization.

Solid boundaries have a no-slip boundary condition for the fluid and a wall-friction law for the crystals, but the majority of fluid and particle motion occurs far from the walls, so boundary conditions have little influence on the dynamics.

Code Validation

The validation of numerical models of dense multiphase mixtures is challenging. This is because granular-fluid mixtures are usually opaque, making optical measurements of laboratory experiments difficult. Inserting instruments into experimental systems would interfere with the flow field by particle-instrument interactions. In addition, the large number of degrees of freedom and many-body interactions produce emergent behavior, non-local and non-affine deformation such as shear-localization, dilatancy and jamming, all of which are not always repeated in duplicate experiments. Laboratory experiments can have multi-modal grain sizes with variable density and roughness, which is hard to duplicate in a numerical model for validation. Hence validation of numerical models for dense multiphase systems is usually based on the statistics of many realizations from an experimental test-bed that recovers the largest scales of the dynamics such as the global properties of mixing, pressure-drop, bed-height, or other measures of system-scale, granular ensemble behavior.

Numerous exercises have been previously performed on the MFIX-DEM code as validation studies (Li *et al.*, 2012). This has included quasi-static granular flow such as run-out to reproduce the repose angle of glass beads, and under more dynamic conditions, simple multiphase shear flow, particle segregation and unmixing, as well as fully fluidized states. MFIX-DEM results and analog experiments gave very good agreement across the entire dynamic range. However we also developed validation exercises.

As our simulations exemplify a dynamic cycle from static to fully-fluidized, we must demonstrate validation for both these states. The Viscous number, I_v , and critical particle volume fraction, $\varepsilon_{c,c}$, framework (defined in the main text) provide a basis for

identifying which dynamic regime and validation protocols are appropriate (Ness & Sun, 2015). The Viscous number is zero in the initial quasi-static regime where the volume fraction is near critical at the random packing of approximately 0.6. In the fully fluidized regime the Viscous number is variable with values spanning more than an order of magnitude and with a variable crystal volume fraction that is below the critical crystal volume fraction.

The validation of the initial quasi-static state where the mixing bowl is first formed was based on replicating the fluidization of granular soils (Alsaydalani & Clayton, 2014). Our model reproduced the same geometry and conditions as the analog experiments, indicating that our implementation of MFI-X-DEM is recovering the quasi-static, viscoplastic, dense phase behavior. In this regime, crystal collisions are unimportant and are primarily frictional. Instead, sustained contact forces produce stress chains and the formation of bounding faults that create the mixing bowl. The formation of these bounding faults is followed by the Reynolds' dilatancy leading to the initiation of fluidization. Our simulations capture this process, in accord with experimental results (Alsaydalani & Clayton, 2014).

After the initial quasi-static response that forms the mixing bowl, four time scales compete to control the subsequent fluidization: one associated with the shearing from the momentum flux, one associated with the relaxation time of the crystal-crystal contacts, one associated with the steady forcing of gravity, and one associated with the dissipation from liquid viscosity. For the values of the Viscous number from our simulations, which is never greater than unity, the fluidized portion of the system is always in a quasi-Newtonian regime. Direct validation for this regime is difficult to obtain as no existing

experiments satisfied all the scaling requirements for verisimilitude. Alternatively, we invoke a previous MFIx validation exercise (Li *et al.*, 2012) of a bubbling fluidized bed as a proxy validation for our fluidized regime, as it has body forces and non-steady behavior. However it is in a more fluidized dynamic regime where the Viscous number is greater, and so the dissipation mechanisms are not going to be weighted the same as they are in our simulations. Nonetheless, that validation exercise, which may in fact be a more challenging validation test example than ours, produced excellent agreement with experiments. In summary, our implementation of MFIx code meets validation as far as can be determined from the existing analog experiments.

REFERENCES

- Alsaydalani, M. O. A. & Clayton, C. R. I. (2014). Internal Fluidization in Granular Soils. *Journal of Geotechnical and Geoenvironmental Engineering* **140**, 4013024.
- Coetzee, C. J. & Els, D. N. J. (2009). Calibration of discrete element parameters and the modelling of silo discharge and bucket filling. *Computers and Electronics in Agriculture* **65**, 198–212.
- Costa, F., Coogan, L. A. & Chakraborty, S. (2010). The time scales of magma mixing and mingling involving primitive melts and melt–mush interaction at mid-ocean ridges. *Contributions to Mineralogy and Petrology* **159**, 371–387.
- Cundall, P. A. & Strack, O. D. L. (1979). A Discrete Numerical Model for Granular Assemblies. *Geotechnique* **29**, 47–65.
- Davidson, J., Tepley III, F., Palacz, Z. & Meffan-Main, S. (2001). Magma recharge, contamination and residence times revealed by in situ laser ablation isotopic analysis of feldspar in volcanic rocks. *Earth and Planetary Science Letters* **184**, 427–442.
- Garg, R., Galvin, J., Li, T. & Pannala, S. (2012a). Open-source MFIx-DEM software for gas–solids flows: Part I—Verification studies. *Powder Technology* **220**, 122–137.
- Garg, R., Galvin, J., Li, T. & Pannala, S. (2012b). Documentation of open-source MFIx–DEM software for gas–solids flows.

- Girard, G. & Stix, J. (2009). Buoyant replenishment in silicic magma reservoirs: Experimental approach and implications for magma dynamics, crystal mush remobilization, and eruption. *Journal of Geophysical Research: Solid Earth* **114**, B08203.
- Li, T., Garg, R., Galvin, J. & Pannala, S. (2012). Open-source MFIx-DEM software for gas-solids flows: Part II — Validation studies. *Powder Technology* **220**, 138–150.
- Li, T. & Guenther, C. (2012). MFIx-DEM simulations of change of volumetric flow in fluidized beds due to chemical reactions. *Powder Technology* **220**, 70–78.
- Nakamura, H. & Watano, S. (2007). Numerical modeling of particle fluidization behavior in a rotating fluidized bed. *Powder Technology* **171**, 106–117.
- Ness, C. & Sun, J. (2015). Flow regime transitions in dense non-Brownian suspensions: Rheology, microstructural characterization, and constitutive modeling. *Physical Review E* **91**, 12201.
- Parks, M. M. *et al.* (2012). Evolution of Santorini Volcano dominated by episodic and rapid fluxes of melt from depth. *Nature Geoscience* **5**, 749–754.
- Paulick, M., Morgeneyer, M. & Kwade, A. (2015). Review on the influence of elastic particle properties on DEM simulation results. *Powder Technology* **283**, 66–76.
- Peng, Z., Doroodchi, E., Luo, C. & Moghtaderi, B. (2014). Influence of void fraction calculation on fidelity of CFD-DEM simulation of gas-solid bubbling fluidized beds. *AIChE Journal* **60**, 2000–2018.
- Richter, F. M., Davis, A. M., DePaolo, D. J. & Watson, E. B. (2003). Isotope fractionation by chemical diffusion between molten basalt and rhyolite. *Geochimica et Cosmochimica Acta* **67**, 3905–3923.
- Ruprecht, P., Bergantz, G. W., Cooper, K. M. & Hildreth, W. (2012). The Crustal Magma Storage System of Volcán Quizapu, Chile, and the Effects of Magma Mixing on Magma Diversity. *Journal of Petrology* **53**, 801–840.
- Rutherford, M. J. (2008). Magma Ascent Rates. *Reviews in Mineralogy and Geochemistry* **69**, 241–271.
- Tsuji, Y., Kawaguchi, T. & Tanaka, T. (1993). Discrete particle simulation of two-dimensional fluidized bed. *Powder Technology* **77**, 79–87.
- Wallace, G. S. & Bergantz, G. W. (2005). Reconciling heterogeneity in crystal zoning data: An application of shared characteristic diagrams at Chaos Crags, Lassen Volcanic Center, California. *Contributions to Mineralogy and Petrology* **149**, 98–112.

Yang, F.-L. & Hunt, M. L. (2006). Dynamics of particle-particle collisions in a viscous liquid. *Physics of Fluids* **18**, 121506.